Low-speed cameras system for 3D-DIC vibration measurements in the kHz range

Paolo Neri[a,*], Alessandro Paoli[a], Armando Viviano Razionale[a], Ciro Santus[a]

[a]*University of Pisa. Department of Civil and Industrial Engineering, Mechanical Division. Largo L. Lazzarino 1, 56122 Pisa, Italy*

Abstract: The digital image correlation (DIC) was used in this paper to obtain full-field measurements of a target vibrating at a frequency higher than the maximum cameras' frame rate. The down-sampling technique was implemented to compensate for the cameras' moderate frame rate, thus getting an accurate displacement acquisition even at 6.5 kHz. Two innovative methods to support the DIC application were introduced. The use of fringe projection (or structured light), initially applied on the sample at rest, reduced the effort and time required for the stereo matching task's solution and improved this setting's accuracy and reliability. Additionally, a new time-domain image filtering was proposed and tested to improve the quality of the obtained DIC maps. In combination with the down-sampling, the effect of this filtering technique was tested in this work at (approx.) 2500 and 6500 Hz by measuring the response of a bladed disk to sinusoidal excitation. Evidence of improved results was observed for both frequencies for amplitudes in the range of 10 µm.

Keywords: *reverse engineering, vibration measurement, digital image correlation, low-speed camera, down-sampling approach, bladed disk*

*Corresponding author: Paolo Neri
Ph. +39 (0)50 2218010 Fax +39 (0)50 2210604
Email address: paolo.neri@dici.unipi.it (P. Neri)

1. Introduction and background

Understanding the dynamic behavior of mechanical components is essential to prevent critical operating working conditions and enhance performance. Various measurement techniques are available to carry out experimental data for capturing the dynamic response of structural parts. Conventional methods use individual contact sensors (e.g., strain gauges and accelerometers). These sensors provide pointwise measurements, and the analysis of broad areas requires the simultaneous use of a significant number of sensors. Moreover, alterations in the modal response could be introduced due to the mass-loading effect, and data transmission represents a concern for rotating regimes. Full-field diagnostic should require measuring a large number of points without modifying the structural response [1].

For this reason, contactless optical techniques have been developed and are progressively replacing contact sensors. Laser Doppler Vibrometry (LDV) and Continuous-Scan Laser Doppler Vibrometry (CSLDV) have become relatively well-established techniques within the research community. LDV uses a laser beam and can measure a vibrating target's velocity along the laser line-of-sight direction by detecting the frequency shift between the reference beam and the beam reflected by the target [1, 2]. However, conventional LDV sensors carry out pointwise measurements, thus making unfeasible the analysis of complex shapes. Some high-end setups have been conceived to cope with the automatization of multiple measurements by an LDV sensor. In [3], for example, a robotic arm was used to automatize the sensor's sequential placement around the object. These approaches, however, are time-consuming as well as costly. CSLDV sensors have been developed to speed up the measurement process by using mirrors to scan whole surfaces, thus providing full-field measurements in a relatively short time [4, 5]. LDV and SLDV approaches are sensitive measurement systems in a broad range of frequencies and can even be applied to small objects. However, these techniques are still limited in the measurement direction and provide mono-dimensional measurements unless three separate sensors are simultaneously used (i.e., Polytec PSV-500-3D [6]), or a single CSLDV is sequentially placed at three different positions to measure structures under steady vibrations to provide 3D velocity information [7]. A further concern is that SLDV sensors carry out sequential and not simultaneous measurements on the target surface. This may lead to inconsistent data in the measurement of vibrations if the excitation load is not synchronously measured, as in this work.

The Digital Image Correlation technique (DIC) can be considered relatively new compared to contact and SLDV sensors. However, its importance has notably increased and in the last few years demonstrated to be a competitive approach to obtain full-field, non-contact characterizations of vibrating targets. DIC is based on processing grayscale variations of random speckle black and white patterns used as marker points, applied on the target surface, and recorded by a digital camera. If two calibrated cameras are used, three-dimensional (3D) coordinates of marker points can be determined by triangulating corresponding 2D points on the stereo image

pairs [8]. 3D point tracking can then be adopted to retrieve 3D displacements of target points, thus collecting structure dynamics information. Recent studies have investigated the possibility of using three-dimensional DIC, referred to as 3D-DIC, to collect the stereo full-field data of vibrating targets. The advent of high-speed cameras characterized by proper resolutions has allowed photogrammetric techniques to explore dynamic phenomena [9]. The most adopted approach consists of using two synchronized cameras [1, 10-12]. Additionally, more complicated setups, consisting of multiple cameras, have been experimented [13]. The high cost of assembling stereoscopic setups with high-resolution high-speed cameras has pushed academic research towards low-cost techniques. Layouts consisting of a single camera, for example, have been experimented to obtain full-field 3D vibration measurements by 3D-DIC [14-17]. A diffraction grating, bi-prisms, or mirrors are used to split the imaged target into two sub-images capturing the scene from two different orientations, thus creating a pseudo-stereo image pair [18]. Compared to 3D-DIC systems composed of two high-speed synchronized cameras, these single-camera setups represent compact, cost-effective solutions. However, the simplicity of a classical stereo setup is complicated by the presence of additional optical elements that, even if compactly arranged, introduces further geometrical constraints. Also, using biprisms or mirrors splits the optical sensor into two halves, thus reducing the field of view and the measurement sensitivity. This issue significantly limits the measurement of high-frequency vibration modes characterized by small deflections of the target object. An alternative approach to reduce costs relies on the definition of stereoscopic setups composed of low frame rate cameras, characterized by high spatial resolution, used with fast exposure times to "*freeze*" a part of the motion. In this case, down-sampled data sets are collected by acquiring images at frequencies lower than vibration loading. In [19], this approach has been used to carry out 3D-DIC measurements up to 1 kHz.

A similar approach has been used in the present paper to develop a stereo optical setup, composed of two conventional low frame rate cameras, which uses 3D-DIC to acquire a full view of the vibrating targets. The two cameras have been integrated with a digital projector to exploit Fringe Projection (FP). The integration between FP and DIC has been already experienced in the technical literature to record full-field displacement maps during vibration experiments of industrial parts [20-22]. However, these approaches have been developed to define a low-cost alternative to 3D-DIC, since a single high-speed camera is combined with a digital projector instead of using stereoscopic camera systems. FP is used to measure out-of-plane displacements, while 2D-DIC is used to determine in-plane displacements. Instead, the approach proposed in the present work uses FP to accomplish stereo matching between images captured by the stereo optical setup, thus enhancing its robustness, especially in correspondence with high curvature regions.

The Nyquist-Shannon frequency limitation is overcome by adopting a down-sampling approach [23, 24], under the hypothesis that a single known frequency component characterizes the excitation signal. A filter is also proposed to enhance measurement sensitivity: since the main harmonic component of the measured signal is

known, a time-domain filter is applied to the acquired images to enhance the relevant harmonic contribution and to reduce the spurious noisy components.

The proposed approach was experimented on the 3D reconstruction of a vibrating bladed disk (namely blisk) and demonstrated to be effective for achieving a relatively low-cost setup for 3D full-field characterization of complex shapes to the range of several kHz. In particular, the presented setup covers frequencies exceeding 6 kHz, which are higher than those reported in [19] but also higher than those experimented by using stereo setups with high-speed cameras [1, 10].

2. Measurement principles

The proposed system is based on the 3D-DIC measurement principle. Two digital cameras are used to take a series of image pairs during a vibrating experiment. This section addresses four main issues: definition of the optical setup, definition of the 3D acquisition strategy, solution of the stereo matching task, and post-processing and filtering of the acquired data.

2.1. Optical setup

The developed 3D acquisition system is based on conventional industrial cameras, which guarantee high resolution at reasonable costs, instead of high-speed cameras. The main drawback is represented by a slower acquisition time, which impairs the system's usability to measure fast transient phenomena. Nevertheless, it was demonstrated that this kind of camera could be suitable for acquiring periodic phenomena, even at frequencies higher than the available frame rate [23]. Two OptoMotive TREX cameras (OptoMotive, Ljubljana, Slovenija, EU) were assembled on a rigid rig to configure a stereo setup. These cameras are characterized by a 1-inch CMOSIS sensor (2024 × 2024 resolution) with a maximum frame rate of 178 fps and a minimum shutter time of 2 μs. It is worth noting that the main limitation to acquire a vibrating target is represented by the shutter time since long exposure times may cause the acquisition of blurred images. In this context, the TREX camera's minimum shutter time represents one-fiftieth of a 10 kHz signal period. Such a short exposure time requires high-intensity illumination. For this reason, four 100 W led modules (Stratus LED module, version 3), equipped with parabolic reflectors, were mounted on the stereo setup rig. Cameras and led modules were mounted on the rig through ball joints and individual sleds to ensure precise orientation. Manfrotto 494BH precision ball joints were used for the cameras to maintain their optical stereo calibration over time. Multifocal 5 Mpixel 1-inch C-mount lenses were adopted (Azure Photonics 1632ZL5M): these lenses allow for varying the settings of parameters like aperture, focus, and focal length, thus providing high flexibility in configuring the working volume. A digital multimedia projector (AAXA P7 led projector, 1920 × 1080 resolution) was also mounted on a bar through a separate sled and ball joint, which is orthogonally fixed to the camera's rig (Fig. 1). This additional degree of freedom allows setting the projector-target distance

independently from the cameras so that the area illuminated by the projector can be adjusted for the cameras' field of view. Figure 1 shows an overview of the described setup.

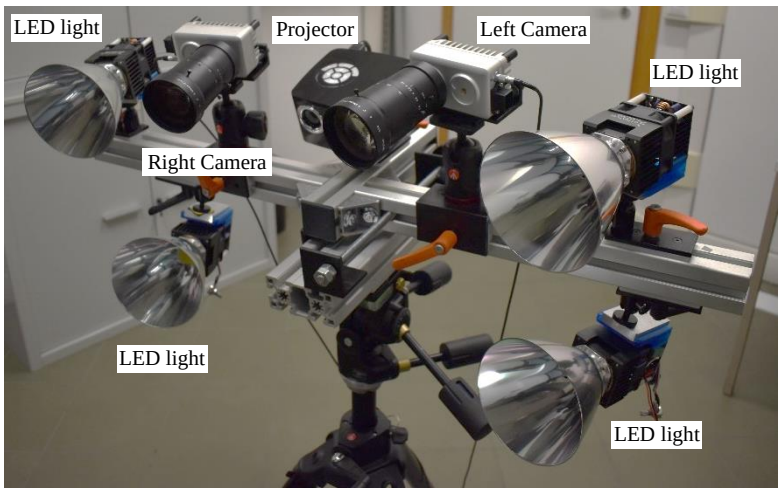

Figure 1 – Experimental setup: stereo-camera system for 3D DIC.

2.2. Measurement approach

2.2.1 Down-sampling strategy

The Nyquist-Shannon theorem's fulfilment would allow the measurement of vibration frequencies up to 89 Hz, given the adopted industrial cameras' maximum frame rate (178 fps). However, it is still possible to acquire higher frequency signals, provided that they contain only a single harmonic contribution of a known frequency. This can be done using a down-sampling approach and exploiting the aliasing phenomenon so that a high-frequency signal is detected as a fictitious low-frequency response. In particular, knowing the signal frequency f_v and selected the number of samples to be acquired n_s, it is always possible to choose an arbitrarily low sampling frequency f_s as:

$$f_s = f_v n_s/(1+n_s k) \quad (1)$$

where the integer k can be set considering that the higher is k, the lower is f_s.

If Eq. 1 is used to acquire n_s samples, the down-sampled signal will appear as a single full period. Figure 2 (a) shows a sinusoidal signal (continuous line), having f_v = 10 Hz, which was down-sampled by setting k = 1 and n_s = 19, thus obtaining f_s = 9.500 Hz (dotted line). As can be noted, only one full period of the fictitious low-frequency signal is acquired. Nevertheless, it is possible to modify Eq. 1 to allow for the acquisition of more than one fictitious period. Indeed, if n_p period must be acquired, the required f_s frequency can be computed by using the following equation:

$$f_s = f_v(n_s/n_p)(1+(n_s/n_p)k) \quad (2)$$

Figure 2 (b) shows, as an example, the same signal of Fig. 2 (a), down-sampled using Eq. 2 and choosing n_p = 2. Two full periods of the fictitious low-frequency signal are acquired, thus providing redundancy in the data, enhancing the measurement robustness. This acquisition strategy can also be fruitfully combined with the time-domain image filtering later described.

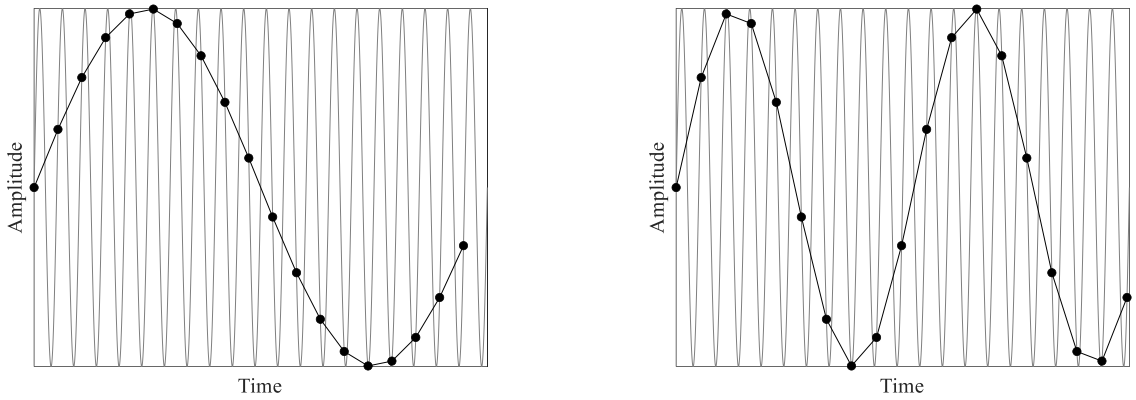

(a) (b)

Figure 2. Different parameters set for the down-sampling procedure: (a) n_p = 1, (b) n_p = 2.

2.2.2 3D-DIC approach

3D-DIC to retrieve the shape of vibrating targets requires solving two tasks. Firstly, the target's displacement field must be computed for each stereo-pair image to obtain 2D information during the vibrating phenomenon. Secondly, corresponding points between the left and right images of each stereo-pair must be determined (stereo matching task) to retrieve 3D information by stereo triangulation. These two tasks could be solved for each stereo-pair image. However, a more suitable strategy to speed up data elaboration consists of solving the stereo-matching problem only for the first pair of images, set as the reference image pair, and then tracking all the corresponding points between frames.

The principle of the adopted 3D-DIC approach is schematized in Fig. 3. Digital image correlation is a subset-based image matching method that uses grayscale values to establish the relationship (correlation) between the two images' subsets. A randomly distributed speckle pattern is sprayed on the target surface to enhance contrast and improve the correlation. A grid of points can be defined on the left image ($grid_{L,0}$), and the DIC algorithm is used to find the corresponding grid points on the right image ($grid_{R,0}$, Fig. 3). This allows computing the 3D coordinates of the points grid on the target surface by exploiting the stereo-triangulation principle. Unfortunately, the traditional DIC method evidences difficulties in matching images when their relative

rotation exceeds 7° [25, 26]. Thus, the definition of a stereo-correlation between left and right camera images using DIC is not trivial since the typical angle of a stereoscopic optical system is about 30°.

For this reason, in this work, a structured light approach, based on the projection of a sequence of vertical and horizontal binary (black and white) striped patterns [27], is proposed to solve the stereo-matching problem. The stereo correlation is solved only once on the reference stereo-pair image at the beginning of the experiment before the vibration is introduced. The DIC algorithm proposed in [28] is then separately used on the temporal sequence of left and right images, respectively, capturing the target surface's deformation from the same orientation.

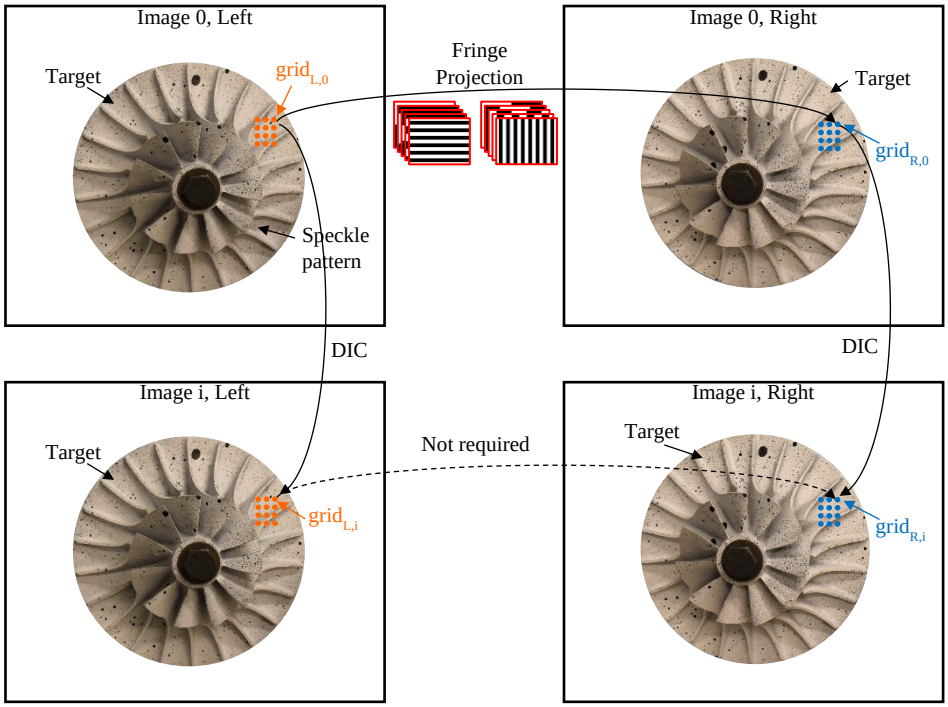

Figure 3 – Scheme of the 3D-DIC approach used for the 3D shape reconstruction.

The fringe patterns are used to define a unique binary code for each point of the acquired left and right images [27]. It is then possible to solve the stereo matching problem by looking for the pixels having the same code in the stereo-pair image. The use of fringe projection is widespread in the scientific literature for 3D surface reconstruction [29]. The method is not typically suitable for moving objects, which prefer one-shot techniques [30], because of its inherent temporal duration. In this work, the multimedia projector projects the binary fringe patterns, while the cameras synchronously acquire the static target surface undergoing structured light. Camera settings can be adjusted in terms of exposure time and frame rate, which do not need to be the same for the vibration measurement step. As an output of the preliminary scanning, a grid of matching points is detected on

both left and right images. This grid can then be directly used for the subsequent DIC elaboration, or down-sampled depending on the desired resolution.

2.3. Time-domain image filtering

The assembled setup is aimed at measuring vibrations in the range of kHz. This is a two-fold challenge in terms of sampling strategy (as described above) and measurement sensitivity. Indeed, high-frequency modes are generally characterized by complex shapes and amplitudes in the range of a few tens of μm. External noise sources could impair the acquisition quality, even if DIC algorithms proved to be suitable for high sensitivity measurements. First of all, random pixel-wise intensity variations, typical of CMOSIS sensors, may even affect almost static acquisitions. Then, any low-frequency external vibration coming from the environment can superimpose to the high-frequency vibration signal. This last occurrence can modify the measurement outcomes, especially in the described down-sampling strategy, which requires a unique sinusoidal component in the vibration signal. These effects cannot be erased entirely, even if they can be mitigated by selecting proper camera settings and environment insulation. Thus, an adequate filtering approach would be advisable.

To this extent, a time-domain filter was developed to be integrated with the proposed down-sampling strategy. The acquired signal comprises n_p full vibration periods if Eq. 2 is used to set the acquisition parameters (i.e., k, n_s, f_s). Thus, the required displacement information in the images will also contain the same number of full periods. Acquired images can then be processed in the time domain to enhance the n_p harmonic component and reduce the noise contribution (random pixel jittering or spurious frequency components). Intensity variation over time can be determined for each ij-th camera pixel. Then the Fast Fourier Transform (FFT) of this signal can be considered, knowing that only the n_p-th component is related to the desired displacement signal. The n_p-th harmonic is preserved, along with the 0-th harmonic (i.e., the mean value), to enhance the expected contribution with respect to the others. All the other harmonics amplitudes are then set to zero, and the inverse FFT is applied. The 0-th harmonic is kept for preserving image features, which are required to properly apply the DIC algorithm on the speckle pattern.

An example of this procedure is presented in Fig. 4. Figure 4 (a) shows the full image of a blisk, which will be further described in the following of the paper. The proposed filtering approach was applied to a high-frequency mode by choosing $n_s = 30$ and $n_p = 1$. Having 30 images, the FFT will provide $h = 30$ harmonics, and the first $h/2$ will be equal to the second $h/2$. Since $n_p = 1$, the displacement information should be related to the first harmonic $h = 1$. A rectangular area in correspondence with one of the blade's tips was selected and zoomed, as shown by the red rectangle in Fig. 4 (a). Figure 4 (b) shows four harmonics, i.e. $h = 0$, $h = 1$, $h = 2$ and $h = 14$, for the pixels in the zoomed area, normalized with respect to the maximum value detected for $h = 1$. The distributions for $h = 3…13$ were skipped since they are substantially equivalent to $h = 2, 14$. As can be

noted by the color scale, the $h = 0$ harmonic, which corresponds to the mean value of the pixels (i.e., the grey level of the static blisk image), has a much higher amplitude with respect to the other harmonics.

On the other hand, the $h = 1$ harmonic has the maximum amplitude if compared with $h = 2, 14$. This confirms that the primary displacement information can be obtained by $h = 1$, while the other harmonics only represent noise. This consideration is further confirmed by the random distribution pattern that characterizes amplitudes for $h = 2...14$, while a clear pattern can be recognized for $h = 1$. Indeed, the higher amplitudes are depicted on the edge of the blade, which experiences the higher displacement for this mode and the black speckles' contour.

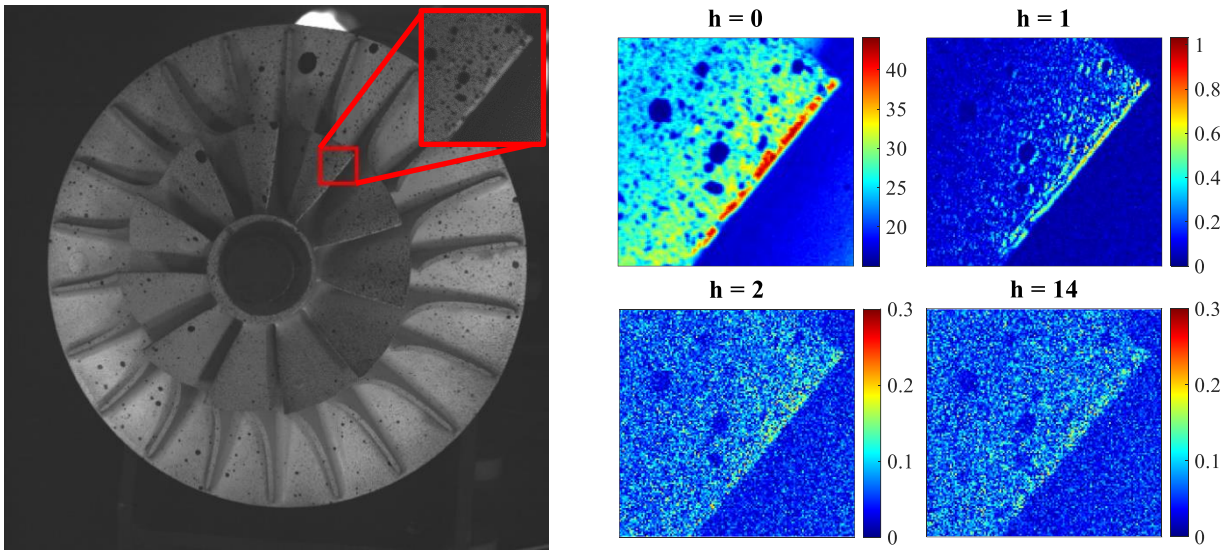

(a) (b)

Figure 4 – Example of the proposed filter to enhance the load harmonic contribution.

Then, the filtered images can be reconstructed by selecting the desired harmonics and performing the inverse FFT. This was firstly carried out by selecting only the $h = 1$ harmonic, showing the results in Fig. 5 (a), and then by choosing both $h = 1$ and $h = 0$ harmonics, Fig. 5 (b). As can be seen, if the mean value is discarded as in Fig. 5 (a), the images' main features are removed (such as the speckle pattern), thus impairing the downstream DIC algorithm performances. On the other hand, if also the $h = 0$ harmonic is selected, the image features are preserved, as shown in Fig. 5 (b), but the higher frequency noise is removed.

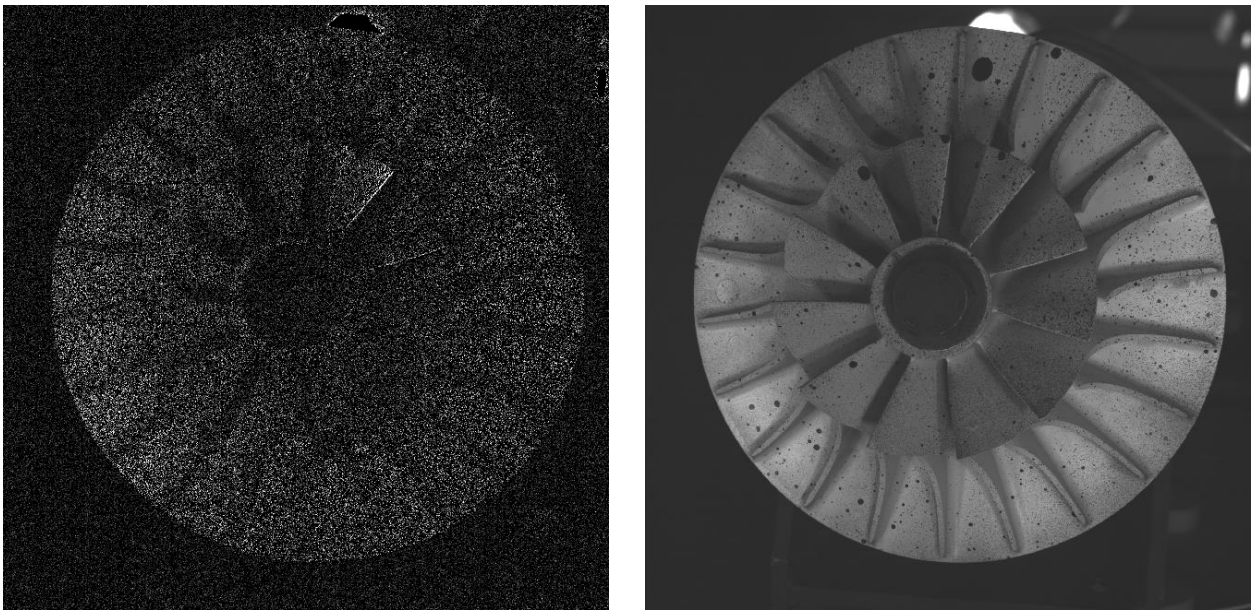

(a) (b)

Figure 5 – Filtered image reconstruction by selecting the harmonics (a) $h = 1$ and (b) $h = 0$ and $h = 1$.

3. Experimental results

A blisk with a diameter of 220 mm has been used for the experimental tests. The blisk has 11 sectors characterized by the presence of splitter blades. The stereo optical setup has been configured for a working volume of $250 \times 250 \times 250$ mm^3 with a baseline (distance between the two cameras) of 265 mm and a working distance of about 650 mm (i.e., the mean distance between the blisk and the cameras), Fig. 6 (a). The excitation system consists of a signal generator (LMS SCADAS), which is used to generate a steady sinusoidal signal at the desired frequency value, a power unit used to amplify the generated signal, and a shaker (TIRAvib TV51110, 100 N peak force), which applies the loading condition. The shaker was directly screwed on the blisk hub. An LDV sensor (Polytec fiber-optic OFV-551) was also used to compute the FFT of single points, thus searching for blisk response peaks. Additionally, Fig. 6 (b) shows the blisk as acquired by the left camera, which is conventionally used to define the measurement reference system.

The proposed structured light approach's performances have been compared to those obtained by solving the stereo-matching task through the Matlab® disparity algorithm. Stereo-pair images are preliminarily rectified by exploiting the camera calibration parameters. A disparity map is then computed from a pair of rectified stereo images using the semi-global matching method [31]. The stereo matching search is reduced to one dimension (epipolar lines become parallel and conjugate points assume the same vertical coordinate, y). This procedure is much faster than conventional 2D-DIC and more robust since the vertical degree of freedom is solved by considering geometrical constraints.

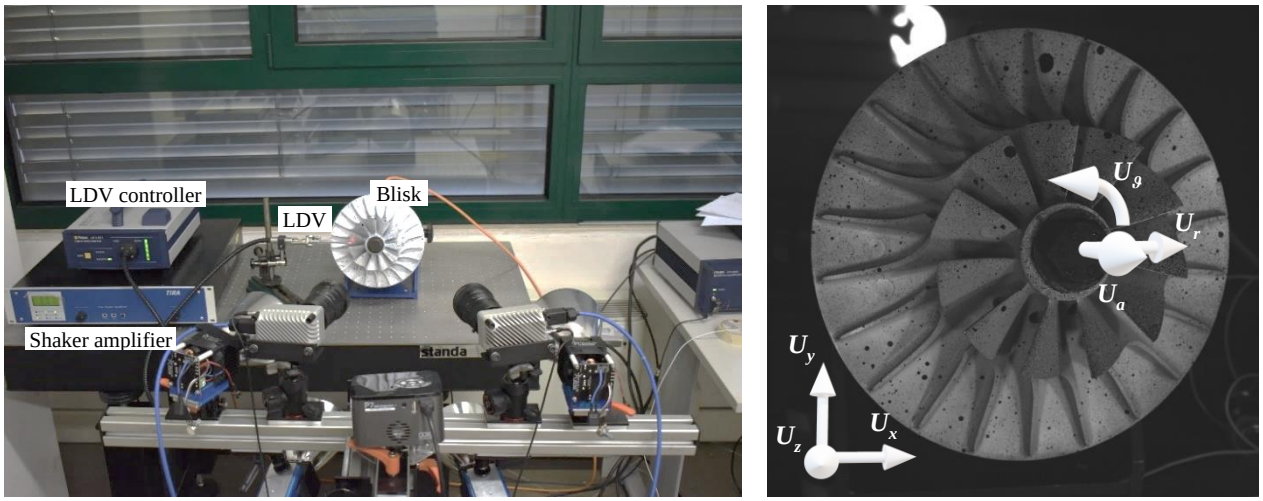

(a) (b)

Figure 6 – Experimental setup: (a) stereo system for 3D-DIC and tested blisk and (b) measurement reference systems.

3.1. Validation of the stereo-matching approach

A two-fold comparison was performed: firstly, regions that were successfully processed by both the stereo matching approaches were analyzed, and secondly, the 3D shapes of the blisk obtained by triangulating the detected corresponding points were compared. The same static blisk pose with respect to the stereo optical setup was used to provide a fair comparison. Figure 7 shows the steps performed to compute the disparity map: Fig. 7 (a) shows the stereo-pair image as acquired by the two cameras, Fig. 7 (b) shows the rectified stereo-pair image, and Fig. 7 (c) shows the obtained disparity map. The disparity range was defined on the rectified stereo-pair image by manually selecting homologous points corresponding to the maximum and minimum distances between the target and the cameras (labels in Fig. 7 (b)). The horizontal coordinate difference determines the disparity range (in this case, [-80, 304] pixels). The results are reported in Fig. 7 (c), where a white rectangle is overlapped to the computed disparity map to highlight the region of interest of the blisk. It is worth noting that the disparity algorithm partially cuts the left side of the blisk since a wide disparity range is needed.

Additionally, the figure highlights that the disparity map was successfully computed for the central screw head, which is flat, and for the disk, which has a low curvature. Only a small portion of the blades, close to the edge, was successfully processed, having a lower curvature. Indeed, the disparity map computation is not trivial when curved surfaces must be processed, resulting in crucial data loss. It is worth noting that the blades' surfaces are of utmost importance in this field since the higher frequency modes mainly involve blade displacements with low disk displacements.

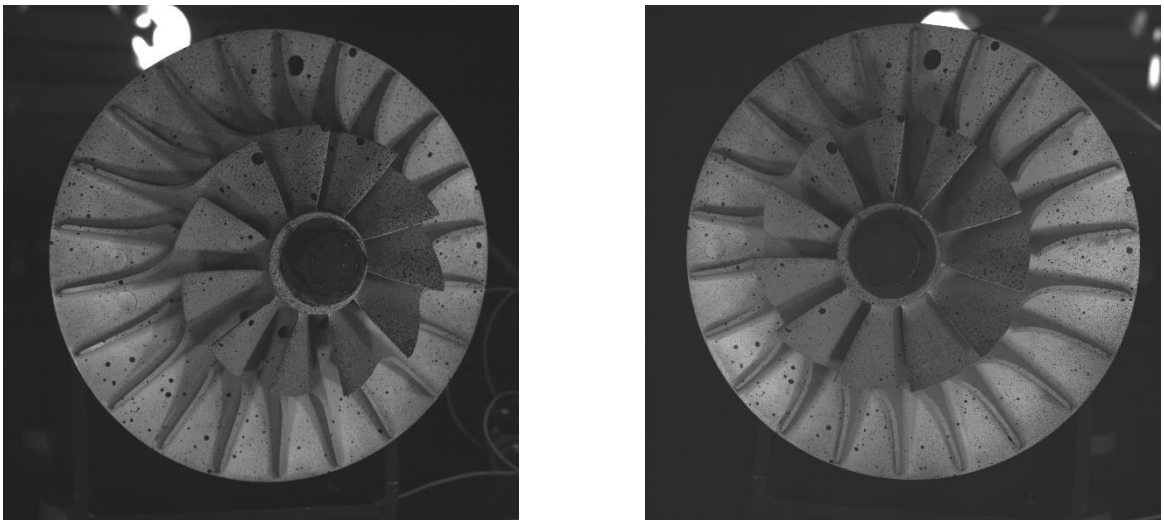

(a)

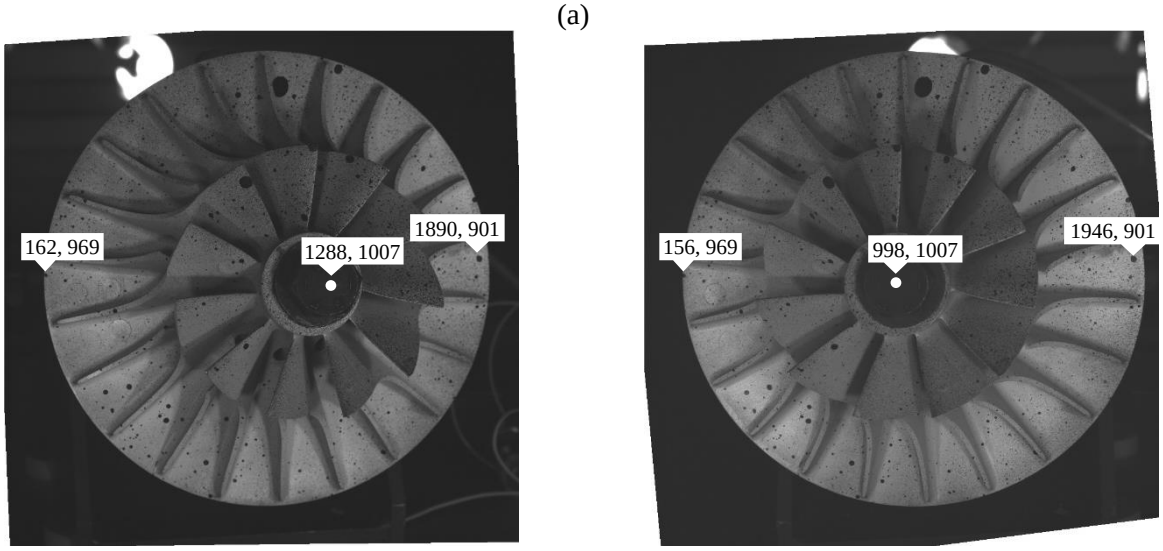

(b)

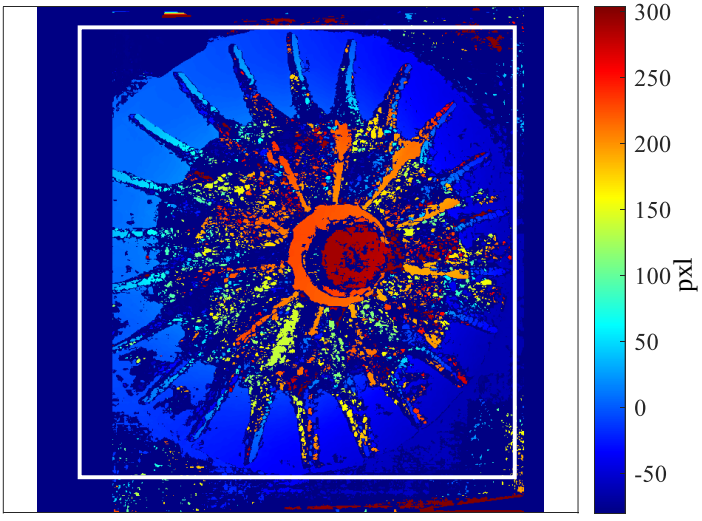

(c)

Figure 7 – Disparity map computation: (a) acquired stereo pair, (b) rectified stereo pair, (c) computed disparity map.

The structured light approach proved to be more robust and reliable to solve the stereo matching task, despite the target surface curvature and texture. A visual comparison between the stereo matching solution provided by the disparity algorithm and the structured light approach is shown in Fig. 8. Figure 8 (a) shows the user-defined grid points on the left image (left side) and their matching points on the right image as detected by the disparity algorithm (right side). The grid on the left image is defined by selecting the region of interest and setting a grid step (e.g., 20 pixels in Fig. 8 (a), determining 8188 points). The grid step can be arbitrarily selected, depending on the desired DIC resolution: finer grid steps can provide higher spatial resolution but much longer computational time. As can be noted, only the points corresponding to the disk and the screw head are correctly matched on the right image. This is further emphasized in Fig. 8 F(c), which shows the 3D reconstruction of the blisk shape, as obtained by triangulating corresponding points.

Figure 8 (d) shows the same grid, as obtained by the structured light approach. It is worth noting that, with this approach, the user does not need to manually define the grid since the measured points are determined at the intersection of the projected fringes. Thus, they are automatically defined by the fringe detection algorithm on both left and right images. Figure 8 (d) was obtained by spatially down-sampling the dense point cloud from the structured light scanning to have a point-to-point distance of about 20 pxl, comparable with the disparity algorithm results. While the complete grid, as defined by the projected fringes, was composed of 18786 points, only 8010 were selected for further processing. As can be noted, the blisk geometry is uniformly covered by the grid, on both left (Fig. 8 (d)) and right (Fig. 8 (e)) images.

Additionally, all the 8010 points of the left grid have a corresponding point on the right image. The only regions of the blisk that are not correctly matched are those visible by only one of the two cameras. These results are confirmed by Fig. 8 (f), which shows the 3D shape reconstruction of the blisk. The plot was obtained using the same view orientation as for Fig. 8 (c) to allow a direct visual comparison of the two point-clouds. The proposed approach, which uses structured light to solve the stereo matching task, provides a much more complete description of the object, also allowing to reconstruct the blades' surface.

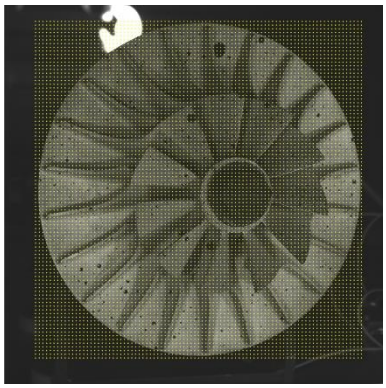

(a)

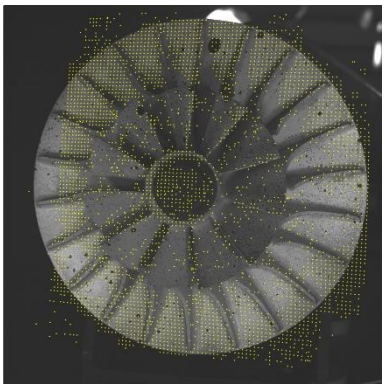

(b)

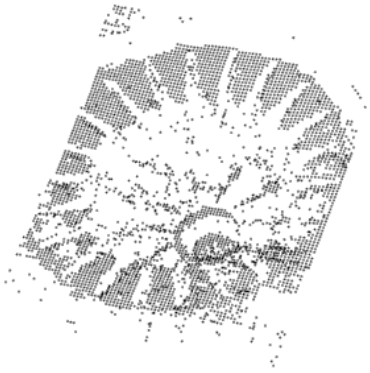

(c)

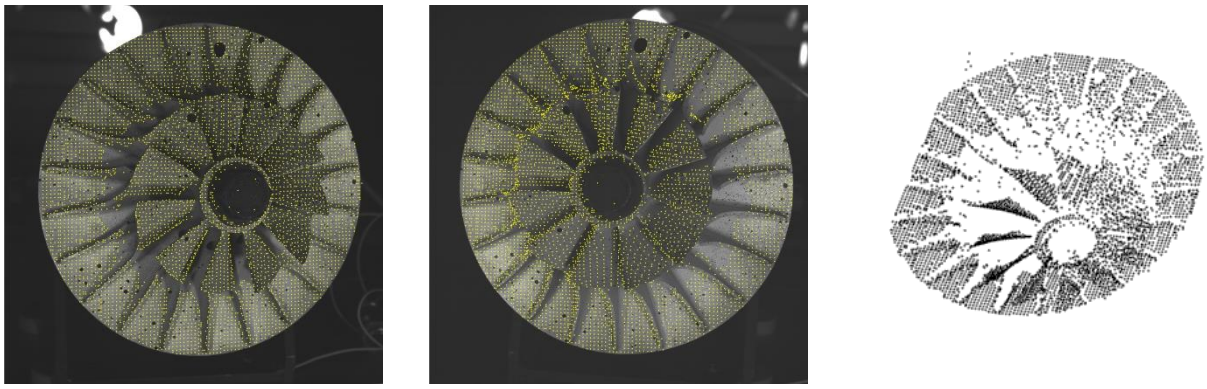

(d) (e) (f)

Figure 8 – Stereo matching solution. Disparity algorithm: (a) user-defined grid on the left image, (b) matching pixels on the right image, (c) 3D reconstructed shape. Structured light algorithm: (d) grid on left image, (e) matching pixels on the right image, (f) 3D reconstructed shape.

3.2. Vibration measurements

After validating the structured light scanning approach to solve the stereo matching task, this section reports vibration measurement results at different frequencies. To this extent, the blisk was preliminarily excited with the shaker with a random signal, in the range 1 – 7 kHz. A single point's response was measured by the LDV sensor, allowing the search for the blisk response peaks (by computing a single point FFT), as shown in Fig. 9.

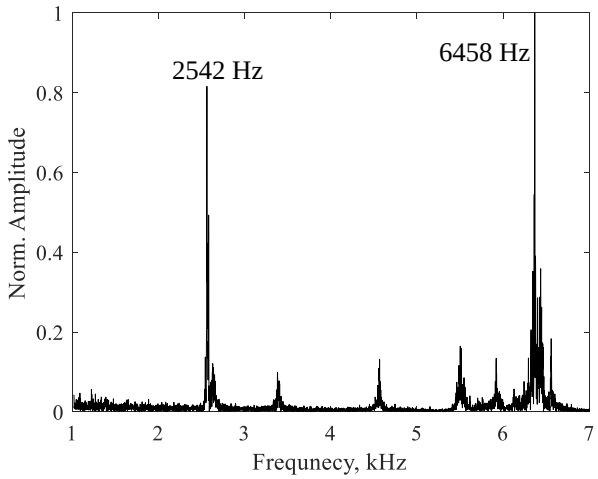

Figure 9 – FFT of the LDV signal of the blisk under random excitation.

Based on the observed peaks, corresponding to the natural modes of the blisk, 3D-DIC measurements were performed at 2542 Hz and 6458 Hz to achieve a full-field description of the deformed shape by setting the cameras frame rate to 10 Hz. Polar coordinates were considered (Fig. 6 (b)) due to the cyclic symmetry of the target object, and radial (U_r), tangential (U_ϑ), and axial (U_a) displacements were computed and mapped. Firstly,

rough data were processed without applying the described time-domain filter. The full-field displacement maps along the three measurement directions for the 2542 Hz frequency are shown in Fig. 10.

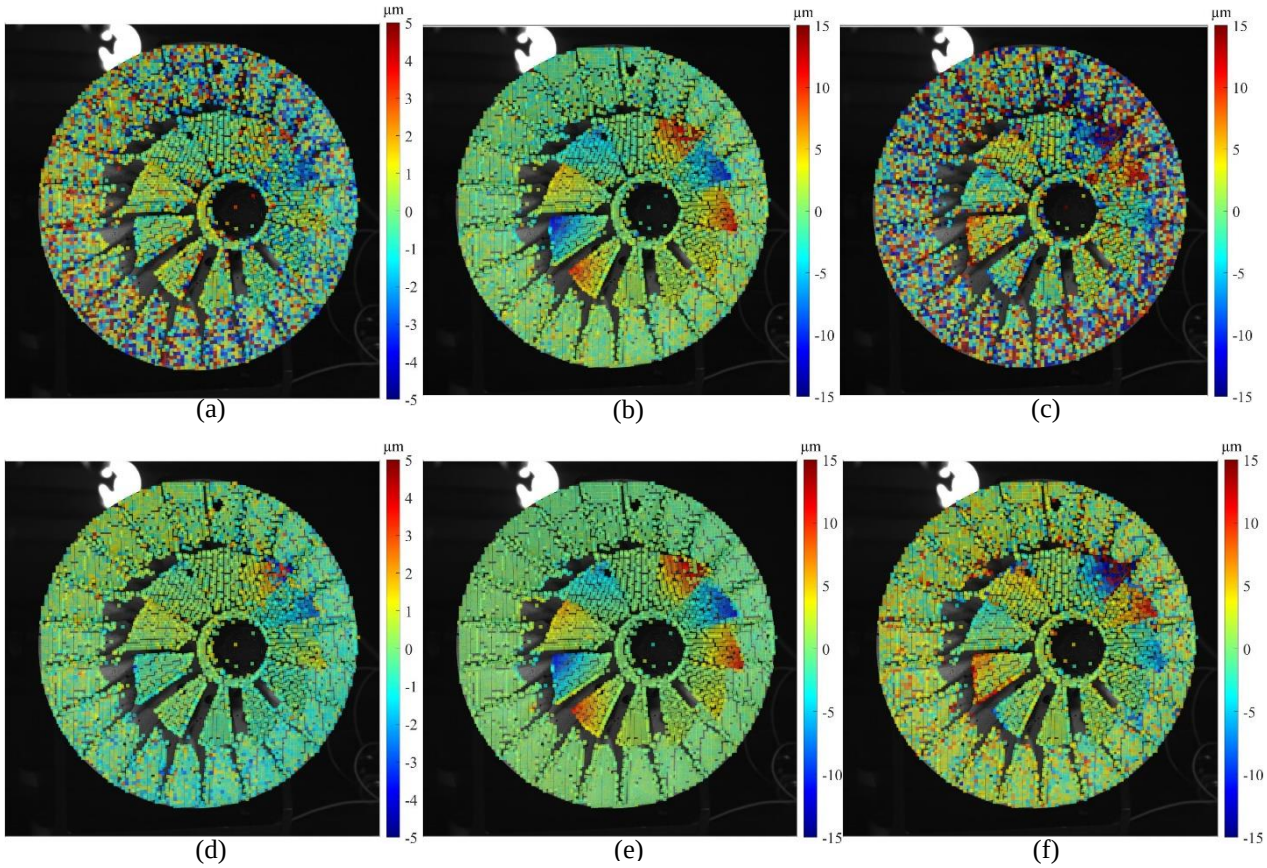

Figure 10 – Deformed shape at 2542 Hz, along the radial, tangential and axial direction respectively: (a), (b), (c) without time-domain filtering of the images, and (d), (e), (f) with the time-domain filtering of the images.

The plot highlights that the 3D full-field displacement map is obtained for the whole blisk, with a maximum amplitude of about 15 µm. Additionally, the comparison between Fig. 10 (a) and (b) shows that, even if the maximum amplitude is almost the same, the measurement noise along the tangential direction is much lower than the noise along the axial direction. This can be mainly ascribed to the fact that the maximum measurement sensitivity is obtained along the direction parallel to the image plane (i.e., radial and tangential). On the other hand, the axial direction (perpendicular to the image plane) is mainly influenced by the stereo-triangulation procedure, which introduces higher noise. Finally, the displacement values over time of a set of points close to the blade tip were extracted and plotted in Fig. 11 (a). Since acquisition parameters were set using Eq.2 and selecting n_p = 1, one period of a sinusoidal signal is expected in the time domain. Indeed, Fig. 11 shows the periodic behavior of the measured signal, even if a significant noise level can be noted in the time domain.

The same images were then processed by exploiting the described time-domain filter. A new filtered image set was then obtained and processed through the DIC algorithm to get the 3D displacement maps. The results

along the three directions are reported in Fig. 10 (d), (e), (f), to be directly compared to Fig. 10 (a), (b), (c). The comparison between Fig. 10 (a), (b), (c) and Fig. 10 (d), (e), (f) evidences that the overall noise level is much lower when the images are pre-filtered with the proposed method. In particular, the displacement maps depicted in Fig. 10 (d) and (f) are much smoother with respect to those reported in Fig. 10 (a) and (c), especially in the areas where the displacement amplitude is low. This result is further confirmed by Fig. 11 (b), which reports the displacement over time of the same points plotted in Fig. 11 (a). Displacements over time are less affected by noise in all the measured directions due to the image pre-filtering process.

The presented measurements demonstrate excellent system performances down to the range of 10 µm and up to the range of 2500 Hz, which are comparable, or slightly better, with respect to the performances of other systems proposed by scientific literature [1, 10, 19]. However, a further response peak was considered at 6458 Hz to assess the system's performance at higher frequencies.

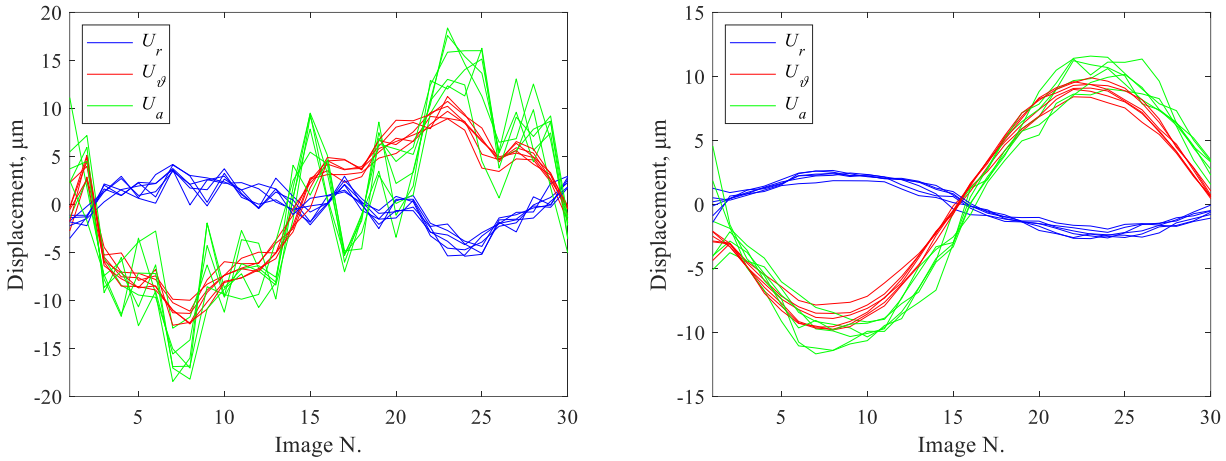

Figure 11 – Displacement over time for the 2542 Hz excitation: (a) without applying the time domain image filtering and (b) applying the time domain image filtering.

The displacement maps corresponding to the three measured directions (without applying the time domain filtering) are reported in Fig. 12 (a), (b), (c), showing that the system can describe the full-field deformed shape. A high noise level can be noted in correspondence with the disk region, which experiences almost zero displacements. Also, the measurement highlights that displacements are mainly localized on a single blade. A complex deformed shape of the blade can be assessed, which is a common feature of high-frequency modes.

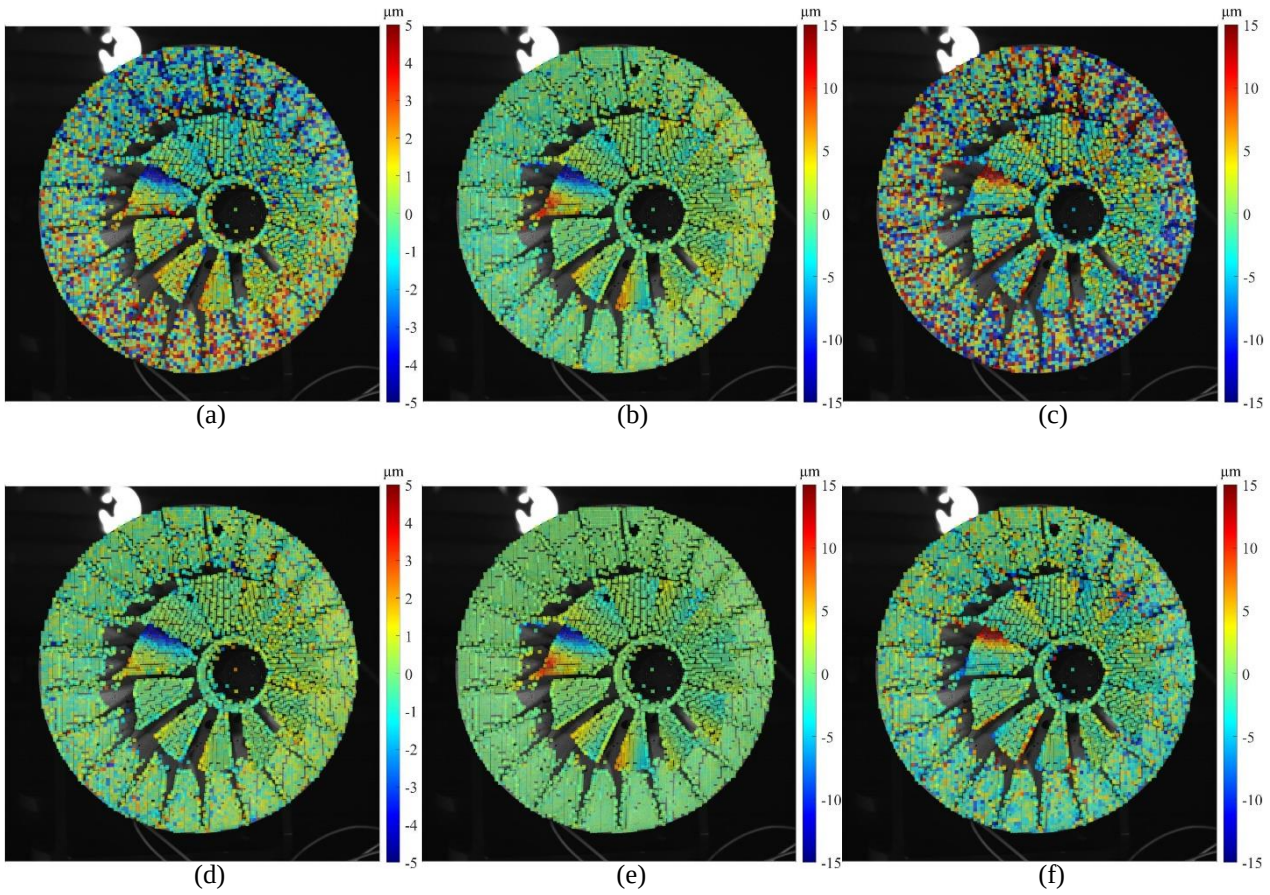

Figure 12 – Deformed shape at 6458 Hz, along the radial, tangential and axial direction respectively: (a), (b), (c) without time-domain filtering of the images, and (d), (e), (f) with the time-domain filtering of the images.

The same image set was then pre-filtered and processed through the DIC algorithm. The results are reported in Fig. 12 (d), (e), (f), which show much smoother maps with respect to those provided in Fig. 12 (a), (b), (c). Fig. 13 plots the displacement values over time of a set of points close to the blade tip for unfiltered (Fig. 13 (a)) and filtered (Fig. 13 (b)) images. In this latter case, the sinusoidal signal is much smoother, thus confirming the time-domain filtering process's effectiveness. It is worth noting that the 6458 Hz response has a higher amplitude with respect to the 2542 Hz test.

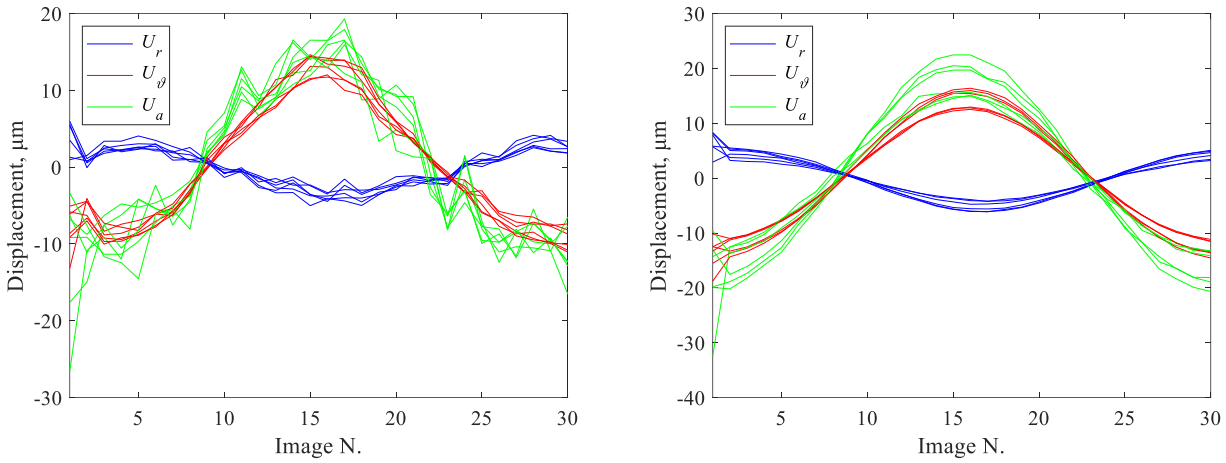

Figure 13 – Displacement over time for the 6458 Hz excitation: (a) without applying the time domain image filtering and (b) applying the time domain image filtering.

Furthermore, Fig. 14 suggests that relevant displacements are measured on all the blades, and not only on the most responsive one. For this reason, the color scale was zoomed to investigate the full-field displacement map further, thus highlighting the presence of displacement values smaller than 5 µm. Results are reported in Fig. 14, which shows the tangential displacement of the blisk obtained by processing the filtered images. As can been seen, all the blades have the same deformed shape, even if with different amplitudes. Furthermore, the blades in the upper half of the blisk move in phase with respect to each other and out of phase with respect to the lower half of the blisk, thus denoting a one nodal diameter mode shape. Additionally, this zoomed color scale enhances the sign reversal along the most responsive blade, thus highlighting the inflection nodal line position.

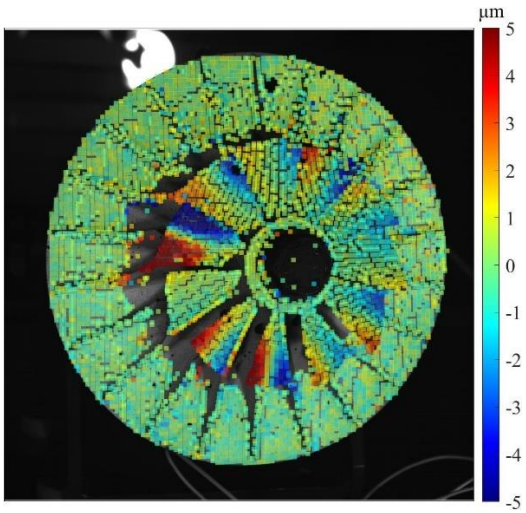

Figure 14 – Tangential deformation at 6458 Hz obtained with the filtered image and a zoomed color scale.

3.3. Validation and discussion

Two steps of validations are proposed for the described measurement method. Firstly, a finite element model of the component was developed, to check if the measured shapes and frequencies were consistent with the numerical results. Nevertheless, blisks are commonly affected by mistuning [32] phenomena, due to any machining inaccuracies which induce the break of the theoretical cyclic symmetry of the system. This implies a slight variation of the natural frequency, however, also a large modification of the mode shapes. The mistuned modes generally become local modes, i.e. mainly involving the deformation of a single blade, or a small number of blades. Even if several methods are available in literature for modelling these phenomena, they are generally based on statistical approaches, thus it is not possible to precisely reproduce the behavior of the specific blisk. For this reason, also an experimental validation was necessary, since the FE model cannot incorporate the mistuning with a predictive approach. An experimental modal analysis was performed by means of a Laser Doppler Vibrometer (Polytec OFV-551). Since the available device was a single-point and 1D sensor, requiring a step by step placing on the desired locations, only one point on each blade was measured. This is a common practice in blisk modal analysis [3], allowing to assess the mistuning level of the component by looking at the mode cyclic asymmetries. Nevertheless, this approach does not allow to achieve a full field description of the shapes in a short time, hence the importance of the developed camera-based system. This procedure was applied to the investigated blisk, and the results corresponding to the high frequency tests are presented for comparison purposes in Fig. 15 (the plots are unitless, since they report eigenvectors).

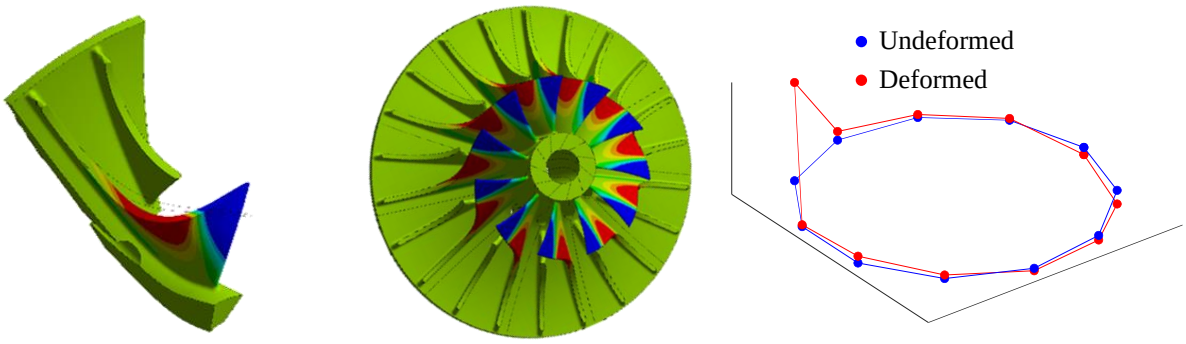

(a) (b) (c)

Figure 15 – Comparison of the results: (a) magnified numerical deformed shape of a blisk sector, (b) numerical displacement along the tangential direction of the full blisk model and (c) LDV detected modal shape with one point per sector along the surface normal.

Figure 15 (a) shows the magnified numerical deformed shape of a single sector. It is evident that the main blade bends with an inflection point, while the disk is approximately still. Figure 15(b) shows the same numerical result for the whole blisk, and the plot orientation was chosen to be comparable with the view in

Fig. 12(e). As can be noted, the deformed shape of the blade is perfectly comparable with the experimental full-field displacement obtained through the proposed method. In addition to that, the difference between the experimental and the numerical frequency was 2.6 %. Nevertheless, the numerical analysis produced a perfect symmetry of the deformed shape, since it appears to be the same for of all the blades (cyclic symmetric analysis and 0 nodal diameter mode was found). On the other hand, the experimental results highlighted high mistuning levels, being the deformation localized mainly on one single blade. This can be verified by looking at Fig. 15(c), which reports the experimental mode shape as measured with the LDV system, by measuring one point per sector close to each of the blade tip along the surface normal. This experimental result confirmed that the actual shape is not symmetric, as depicted by the full-field results (Fig. 12 (e)). Nevertheless, it is worth noting that this latter experimental test required the placing of the measurement sensor in eleven different locations for a testing time of approximately 1 hour. The proposed DIC methodology, instead, required only approximately 10 seconds for the acquisition, resulting in a 3D full-field description of the deformed shape, instead of a localized 1D measurement such as the LDV. Despite these mentioned advantages with respect to conventional measurement techniques, it is crucial to point out that the presented DIC approach needs the excitation source to be characterized by a single sinusoidal component. This is due to the adopted down-sampling approach, which does not allow to measure generic signals, such as random vibrations or combined excitation sources.

4. Conclusions

In this paper, the 3D-DIC method was applied to a bladed disk with a complex shape, leading to challenging vibration displacement distributions. During the setup, the projection of fringes on the object, according to an optimized scheme, significantly improved the accuracy and the easiness of detecting corresponding points between the two cameras. Experimental measurements confirmed that the proposed structured light approach performs better than the conventional correlation approach. It is worth noting that, even if structured light techniques are well known in literature, this is the first time that they are applied to solve the stereo-matching problem in a DIC setup, thus pushing forward this research field. An innovative filter was also proposed for the DIC processing in combination with the down-sampling technique. The left and the right camera images were initially filtered according to the time variable by imposing a sinusoidal function for each pixel, knowing that the time response is a pure harmonic. After introducing this filtering, DIC was performed, and more accurate and regular displacement maps were obtained. This demonstrated that the down-sampling approach, which indeed was already experimented in previous research, can benefit from the proposed time domain filtering, if the proposed Eq. 2 is used to set the testing parameters. Two test frequencies were considered: 2542 Hz and 6458 Hz, corresponding to previously experimentally detected structural resonances. As mentioned before, the down-sampling technique was crucially used in this work. In principle, any vibration

frequency could be captured employing the down-sampling, just provided that the displacement time dependence is perfectly sinusoidal. However, the camera shutter time introduces a limit to the effectiveness of the down-sampling. The 2 μs shutter time of the TREX camera was used here, and vibrations up to 6.5 kHz were accurately resolved to an amplitude lower than 5 μm, which demonstrates a great improvement with respect to the state of the art in this research field. The proposed measurement approach was validated through comparison with numerical and independent experimental results. The Finite Element analysis agreed with the local bending shape of the main blade, while the Laser Doppler Vibrometer measurements confirmed that the component is affected by significant mistuning levels, as typical for this kind of components, especially at high frequencies. Additionally, the 3D full-field measurement obtained with the proposed approach required approximately 10 s of measurement time, which is much shorter with respect to the LDV measurement (approximately 1 hour).

The full-field 3D-DIC maps of the blisk at the 6458 Hz frequency evidenced a nodal line on the upper edge of the blades, while a more uniform deflection was obtained for the 2542 Hz frequency. This global information cannot be easily obtained with a single point measurement and can provide clear indications of the actual bladed disk vibration behavior. The main limitation of the proposed method is the constraint of having only a single sinusoidal component excitation, which allows the down-sampling approach to work properly. This limitation restricts the use of the method to laboratory conditions, where the excitation is typically imposed through an electrodynamic shaker, being precisely controllable. Future developments will investigate the possibility of overcoming this limitation, extending the measurement capabilities to a non-single harmonic signal.

Acknowledgments

The authors are grateful to the University of Pisa for supporting this research activity (Grant PRA_2018_80).

References

[1] P.L. Reu, D.P. Rohe, L.D. Jacobs, Comparison of DIC and LDV for practical vibration and modal measurements, Mech Syst Signal Pr, 86 (2017) 2-16.
[2] J. Baqersad, P. Poozesh, C. Niezrecki, P. Avitabile, Photogrammetry and optical methods in structural dynamics - A review, Mech Syst Signal Pr, 86 (2017) 17-34.
[3] L. Bertini, P. Neri, C. Santus, A. Guglielmo, Automated Experimental Modal Analysis of Bladed Wheels with an Anthropomorphic Robotic Station, Exp Mech, 57 (2017) 273-285.
[4] D. Di Maio, D.J. Ewins, Applications of continuous tracking SLDV measurement methods to axially symmetric rotating structures using different excitation methods, Mech Syst Signal Pr, 24 (2010) 3013-3036.
[5] D.A. Ehrhardt, M.S. Allen, S.F. Yang, T.J. Beberniss, Full-field linear and nonlinear measurements using Continuous-Scan Laser Doppler Vibrometry and high speed Three-Dimensional Digital Image Correlation, Mech Syst Signal Pr, 86 (2017) 82-97.

[6] Polytec, Polytec 3D Scanning Vibrometers (PSV-3D). https://www.polytec.com/us/vibrometry/products/full-field-vibrometers/psv-500-3d-scanning-vibrometer/, 2020 (accessed November 2020).
[7] D.M. Chen, W.D. Zhu, Investigation of three-dimensional vibration measurement by a single scanning laser Doppler vibrometer, Journal of Sound and Vibration, 387 (2017) 36-52.
[8] Y. Gao, T. Cheng, Y. Su, X.H. Xu, Y. Zhang, Q.C. Zhang, High-efficiency and high-accuracy digital image correlation for three-dimensional measurement, Opt Laser Eng, 65 (2015) 73-80.
[9] T.J. Beberniss, D.A. Ehrhardt, High-speed 3D digital image correlation vibration measurement: Recent advancements and noted limitations, Mech Syst Signal Pr, 86 (2017) 35-48.
[10] M.N. Helfrick, C. Niezrecki, P. Avitabile, T. Schmidt, 3D digital image correlation methods for full-field vibration measurement, Mech Syst Signal Pr, 25 (2011) 917-927.
[11] R. Hunady, P. Pavelka, P. Lengvarsky, Vibration and modal analysis of a rotating disc using high-speed 3D digital image correlation, Mech Syst Signal Pr, 121 (2019) 201-214.
[12] A.J. Molina-Viedma, L. Felipe-Sese, E. Lopez-Alba, F.A. Diaz, 3D mode shapes characterisation using phase-based motion magnification in large structures using stereoscopic DIC, Mech Syst Signal Pr, 108 (2018) 140-155.
[13] P. Poozesh, J. Baqersad, C. Niezrecki, P. Avitabile, E. Harvey, R. Yarala, Large-area photogrammetry based testing of wind turbine blades, Mech Syst Signal Pr, 86 (2017) 98-115.
[14] L.P. Yu, B. Pan, Single-camera high-speed stereo-digital image correlation for full-field vibration measurement, Mech Syst Signal Pr, 94 (2017) 374-383.
[15] L.P. Yu, B. Pan, Full-frame, high-speed 3D shape and deformation measurements using stereo-digital image correlation and a single color high-speed camera, Opt Laser Eng, 95 (2017) 17-25.
[16] P. Castellini, P. Chiariotti, M. Martarelli, E. Zappa, A. Lavatelli, Experimental Modal Analysis on Vibration Data Measured by Digital Image Correlation, C Proc Soc Exp Mech, (2017) 285-291.
[17] E. Lopez-Alba, L. Felipe-Sese, S. Schmeer, F.A. Diaz, Optical low-cost and portable arrangement for full field 3D displacement measurement using a single camera, Meas Sci Technol, 27 (2016).
[18] B. Pan, L.P. Yu, Q.B. Zhang, Review of single-camera stereo-digital image correlation techniques for full-field 3D shape and deformation measurement, Science China-Technological Sciences, 61 (2018) 2-20.
[19] J.R. Warburton, G. Lu, T.M. Buss, H. Docx, M.Y. Matveev, I.A. Jones, Digital Image Correlation Vibrometry with Low Speed Equipment, Exp Mech, 56 (2016) 1219-1230.
[20] L. Felipe-Sese, F.A. Diaz, Damage methodology approach on a composite panel based on a combination of Fringe Projection and 2D Digital Image Correlation, Mech Syst Signal Pr, 101 (2018) 467-479.
[21] L. Felipe-Sese, A.J. Molina-Viedma, E. Lopez-Alba, F.A. Diaz, FP plus DIC for low-cost 3D full-field experimental modal analysis in industrial components, Mech Syst Signal Pr, 128 (2019) 329-339.
[22] A.J. Molina-Viedma, L. Felipe-Sese, E. Lopez-Alba, F.A. Diaz, Comparative of conventional and alternative Digital Image Correlation techniques for 3D modal characterisation, Measurement, 151 (2020).
[23] S. Barone, P. Neri, A. Paoli, A.V. Razionale, Low-frame-rate single camera system for 3D full-field high-frequency vibration measurements, Mech Syst Signal Pr, 123 (2019) 143-152.
[24] R.K. Fruehmann, J.M. Dulieu-Barton, S. Quinn, J.P. Tyler, The use of a lock-in amplifier to apply digital image correlation to cyclically loaded components, Opt Laser Eng, 68 (2015) 149-159.
[25] P.-C. Hung, A.S. Voloshin, In-plane strain measurement by digital image correlation, Journal of the Brazilian Society of Mechanical Sciences and Engineering, 25 (2003) 215-221.
[26] R. Wu, D.S. Zhang, Q.F. Yu, Y.X. Jiang, D. Arola, Health monitoring of wind turbine blades in operation using three-dimensional digital image correlation, Mech Syst Signal Pr, 130 (2019) 470-483.
[27] S. Barone, P. Neri, A. Paoli, A.V. Razionale, 3D acquisition and stereo-camera calibration by active devices: A unique structured light encoding framework, Opt Laser Eng, 127 (2020).
[28] C. Eberl, Digital Image Correlation and Tracking, Mathworks, Matlab Central, 2010.
[29] C. Zuo, S.J. Feng, L. Huang, T.Y. Tao, W. Yin, Q. Chen, Phase shifting algorithms for fringe projection profilometry: A review, Opt Laser Eng, 109 (2018) 23-59.
[30] S. Zhang, High-speed 3D shape measurement with structured light methods: A review, Opt Laser Eng, 106 (2018) 119-131.
[31] H. Hirschmuller, Accurate and efficient stereo processing by semi-global matching and mutual information, Proc Cvpr Ieee, (2005) 807-814.
[32] P. Neri, L. Bertini, C. Santus, A. Guglielmo, Generalized SAFE Diagram for Mistuned Bladed Disks, J Eng Gas Turb Power, 141 (2019).